RSC Pharmaceutics

ROYAL SOCIETY OF CHEMISTRY

PAPER

View Article Online
View Journal | View Issue

Cite this: *RSC Pharm.*, 2025, **2**, 598

Comparative evaluation of cocrystalline and coamorphous forms comprised of gefitinib and dasatinib for performance optimization†

Xian-Bi Shi,[a] Zhi-Qing Wang,[a] Hui-Tian Li,[b] Xia-Lin Dai,[b] Xiang-Tian Long,*[c] Yong-Liang Huang,[d] Jia-Mei Chen *[b] and Tong-Bu Lu [a]

Drug–drug cocrystals and coamorphous systems, both comprising two drugs in a single phase, can be applied to concurrently improve the physicochemical properties of the involved drugs. The comparative evaluation of cocrystalline and coamorphous forms comprised of a given drug combination aid in finding the optimal solid form for the development of synergistic formulations. Gefitinib (GTB) and dasatinib (DAS) are oral tyrosine kinase inhibitors exhibiting synergistic effects against cancer cells. However, they both belong to BCS II drugs showing solubility that differ by several times. To optimize the performance of hybrid drugs, one cocrystal (**GTB-DAS·2H$_2$O**) and one coamorphous solid form (**GTB-DAS CM**) were successfully prepared and fully characterized by XRD, ^{1}H NMR, TG, DSC, FTIR and DVS measurements. Crystal structural and Hirshfeld surface analysis shows GTB molecular layers are intercalated with layers of DAS *via* van der Waals interactions and weak hydrogen bonding interactions in the cocrystal. The stability and tabletability properties of **GTB-DAS·2H$_2$O** and **GTB-DAS CM** were evaluated, and the dissolution performance was studied in terms of T_{max} (time to peak drug concentration), C_{max} (maximum drug concentration) and AUC (area under the curve of dissolution profiles). Overall, **GTB-DAS·2H$_2$O** shows superior stability and tabletability properties, and synchronized drug release with improved dissolution performance, making it a more promising and reliable solid form for the development of combinational therapy.

Received 21st August 2024,
Accepted 20th January 2025

DOI: 10.1039/d4pm00237g

rsc.li/RSCPharma

1. Introduction

The combination of multiple drugs has become an emerging drug development strategy for the treatment of many complex diseases, such as HIV/AIDS, cancer, cardiovascular disease, *etc*.[1,2] The drug combinations exhibit numerous advantages such as synergistic effects, reduced adverse events and drug resistance, good patient compliance and lower managerial and manufacturing costs compared with monotherapy.[3–5] However, the development of drug combinations usually suffers from issues on incompatibility of stability and solubility of parent drugs, which seriously restrict their advantages and bring about huge risks.[6,7] Drug–drug cocrystalline and coamorphous systems, both comprising two drugs in a single phase, have the potential to concurrently improve the physicochemical properties of the involved drugs, and can be applied to address the aforementioned issues to facilitate the development of combination therapies.[8–11] Several commercial drug–drug cocrystalline products have already been approved (*e.g.* Gravol®, Dichloralphenazone®, and Entresto®),[12–14] and some examples of drug–drug coamorphous systems have already been reported.[15–18] However, little investigation has yet been carried out on systematically comparing physicochemical characteristics of cocrystalline and coamorphous forms consisting of a given drug combination, with the intention to find the optimal solid form for the development of synergistic formulations.[19]

Gefitinib (GTB, Scheme 1) is an oral tyrosine kinase inhibitor marketed for patients with non-small cell lung cancer treatment.[20] However, the clinical efficacy of GTB is limited due to its acquired resistance after nine to twelve months of treatment.[21] Dasatinib (DAS, Scheme 1) is an oral multi-targeted tyrosine kinase inhibitor for the treatment of chronic myelogenous leukemia.[22] The combination of DAS and GTB has been evaluated on GTB-resistant lung cancer cells and shows enhanced killing effects.[23] The DAS and GTB combi-

[a]*Institute for New Energy Materials and Low Carbon Technologies, School of Materials Science and Engineering, Tianjin University of Technology, Tianjin 300384, China*
[b]*School of Chemistry and Chemical Engineering, Tianjin University of Technology, Tianjin 300384, China. E-mail: chenjiamei@email.tjut.edu.cn*
[c]*Tasly Academy, Tasly Holding Group Co., Ltd, Tianjin 300410, China. E-mail: njulxt@163.com*
[d]*Department of Chemistry, Shantou University Medical College, Shantou, Guangdong 515041, China*

†Electronic supplementary information (ESI) available. CCDC 2330839–2330841. For ESI and crystallographic data in CIF or other electronic format see DOI: https://doi.org/10.1039/d4pm00237g

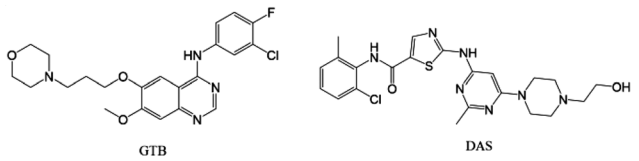

Scheme 1 Chemical structures of gefitinib (GTB) and dasatinib (DAS).

nation also represents a promising new therapeutic modality for ovarian cancer.[24,25] Both GTB and DAS belong to the class II drugs of the biopharmaceutical classification system, and their solubility differs by several times.[26,27] This may lead to incompatibility issues of the hybrid drugs, and subsequently impact the exertion of their synergistic effect for cancer treatment.

To optimize the performance of hybrid drugs and facilitate the development of combination therapies, we report multi-component solid forms involving GTB and DAS that can exist both in cocrystalline and coamorphous states. The obtained cocrystal and coamorphous system has been fully characterized by XRD, ^{1}H NMR, TG, DSC, FTIR and DVS measurements. Crystal structural and Hirshfeld surface analysis of the cocrystal was carried out to help understand the role and significance of different types of intermolecular interactions responsible for crystal packing. The amorphization of GTB-DAS was confirmed as a halo pattern in PXRD measurements and a single glass transition event in the DSC curves. The stability and tabletability properties of cocrystalline and coamorphous solid forms were evaluated, and the dissolution performance was studied in terms of T_{max} (time to peak drug concentration), C_{max} (maximum drug concentration) and AUC (area under the curve of dissolution profiles), aiming to find the optimal solid form for the development of synergistic formulations.

2. Materials and methods

2.1 Materials

GTB and DAS were purchased from Shanghai Shengde Chemical Co. Ltd (China). All other chemicals and solvents were obtained from various commercial sources and used without further purification.

2.2 Preparation and characterization

2.2.1 Preparation of GTB-DAS·2H$_2$O (1 : 1 : 2). **GTB-DAS·2H$_2$O** was obtained by the following three methods. (I) A liquid-assisted milling method was used for cocrystal screening. A powdered mixture of GTB (8.9 mg, 0.02 mmol) and DAS·H$_2$O (10.1 mg, 0.02 mmol) was ground with 10 μL of methanol using a Retsch MM 400 mixer mill at a frequency of 20 Hz for 30 min. (II) A rapid evaporation method was used for cocrystal screening. A powdered mixture of GTB (8.9 mg, 0.02 mmol) and DAS·H$_2$O (10.1 mg, 0.02 mmol) was added to 30 mL of anhydrous methanol, and the resulting suspension was stirred at 40 °C until the solids were completely dissolved. The solution was naturally cooled and filtered. The filtrate was treated using a rotary evaporator to quickly remove the solvent. (III) A slurry method was used to prepare bulk samples for characterization and property evaluation. An equimolar mixture of GTB (89.1 mg, 0.2 mmol) and DAS·H$_2$O (101.2 mg, 0.2 mmol) was added to a solvent mixture of 2 mL *n*-heptane and 100 μL methanol and was then stirred for 24 h at room temperature. The resulting suspension was filtered and the obtained white solid was dried under air. Yield: 172.4 mg, 87.2%.

2.2.2 Preparation of single crystals. Powder of **GTB-DAS·2H$_2$O** (9.6 mg, 0.01 mmol) was added to 4 mL of methanol and treated by ultrasound. The resulting solution was filtered and the filtrate was then allowed to evaporate at room temperature. Colorless rod-shaped single crystals of **GTB-DAS·2H$_2$O** (1 : 1 : 2) were obtained after 3–4 days. A powdered mixture of GTB (4.5 mg, 0.01 mmol) and DAS·H$_2$O (5.1 mg, 0.01 mmol) was added to 4 mL of mixed solvent of methanol and water with a volume ratio of 1/1 and then treated by ultrasound. The resulting solution was filtered and the filtrate was then allowed to evaporate slowly at 4 °C. Colorless rod-shaped single crystals of **GTB-DAS·2MeOH** (1 : 1 : 2) or **GTB-DAS** (1 : 1) were obtained after 3–4 days.

2.2.3 Preparation of amorphous and coamorphous forms. Powder of GTB (1 g) or DAS·H$_2$O (1 g) or an equimolar mixture of GTB and DAS·H$_2$O (1.0 g sample in total) were ground using a Retsch MM 400 mixer mill at a frequency of 25 Hz for up to 180 min with a cool-down period of 20 min after every 30 min.

2.2.4 ^{1}H nuclear magnetic resonance (^{1}H NMR). ^{1}H NMR spectra were acquired on a Bruker Avance III 400 MHz spectrometer using dimethyl sulfoxide-d6 as the solvent and TMS (0 ppm) as the internal standard.

2.2.5 Single-crystal X-ray diffraction. Single-crystal X-ray diffraction data were collected on an Agilent Technologies Gemini A Ultra system with graphite monochromated Cu Kα radiation (λ = 1.54178 Å). Cell refinement and data reduction were applied using the program CrysAlis^{Pro}. The structure was solved by the direct method using the Olex2 program and refined by the full-matrix least-squares method on F^2. All non-hydrogen atoms were refined with anisotropic displacement parameters. All hydrogen atoms were placed in calculated positions with fixed isotropic thermal parameters and included in the structure factor calculations in the final stage of full-matrix least-squares refinement.

2.2.6 Hirshfeld surface analysis. Hirshfeld surface analysis based on single-crystal structures was performed using the Crystal Explorer 17.5 program. The distances were plotted from the Hirshfeld surface to the nearest nucleus outside (d_e) and inside (d_i) the surface. The contributions of various types of interactions between atoms were calculated from the normalized contact distance d_{norm}.

2.2.7 Powder X-ray diffraction (PXRD). The room temperature PXRD data were obtained on a Rigaku Mini Flex 600 with Cu Kα radiation (λ = 1.541862 Å) at 40 kV and 15 mA. The data were recorded in continuous scan mode with a step size of

0.01° (2θ) and a scan speed of 20° min^{-1}. The variable temperature PXRD data of **GTB-DAS·2H$_2$O** were collected on a Bruker D8 ADVANCE DAVINCI instrument connected to an Anton Paar non-environmental stage. Data with a step size of 0.01° and a sweep speed of 20° min^{-1} were collected using Cu Kα radiation (λ = 1.5418 Å) and a Lynxeye XE detector at different temperatures (25 °C, 100 °C, 120 °C, 140 °C, 145 °C, 160 °C, 180 °C, 200 °C, and then back to 25 °C).

2.2.8 Thermogravimetric (TG) analysis. TG data were recorded on a Netzsch TG209 F3 instrument. Each sample was placed in a sample pan and heated over the temperature range of 40–500 °C at a heating rate of 10 °C min^{-1}.

2.2.9 Differential scanning calorimetry (DSC). DSC measurements were conducted on a Netzsch DSC 214 instrument under a nitrogen atmosphere. Each sample was sealed into an aluminium pan and heated at a heating rate of 10 °C min^{-1}. For the modulated DSC (MDSC) measurements, each sample was crimp-sealed in an aluminium pan with three pin holes. The measurement was recorded between 25 and 250 °C at a heating rate of 2 °C min^{-1} with a modulation amplitude of ±0.5 °C and a modulation period of 60 s. The collected data were examined using Netzsch Proteus thermal analysis software to determine the experimental T_g values (midpoint of the reverse heat-flow signal). Each amorphous and coamorphous sample was analysed over three independent measurements (n = 3) to calculate the mean values and standard deviations.

2.2.10 Theoretical calculations on T_g. The theoretical T_g value of the coamorphous system was calculated using eqn (1),

$$T_{g(mix)} = \frac{W_1 \cdot T_{g1} + K \cdot W_2 \cdot T_{g2}}{W_1 + K \cdot T_{g2}} \quad (1)$$

where $T_{g(mix)}$ (in K) is the glass transition temperature of **GTB-DAS CM**, and W_1, T_{g1} (in K) and W_2, T_{g2} (in K) are the weight fractions and glass transition temperatures of pure amorphous GTB and DAS, respectively. K is a constant and calculated using eqn (2),

$$K = \frac{\rho_1 \cdot T_{g1}}{\rho_2 \cdot T_{g2}} \quad (2)$$

where ρ_1 and ρ_2 are respective powder densities of the single amorphous components (1.3172 ± 0.0009 g cm^{-3} for GTB, 1.3212 ± 0.0007 g cm^{-3} for DAS).

2.2.11 True density test. The true density test was performed on an AccuPyc II 1345 fully automated densitometer from Micromeritics, USA, repeating the test 5 times and taking the average of the 5 results.

2.2.12 Fourier transform infrared (FTIR) spectroscopy. FTIR spectra were recorded on a ThermoFisher Scientific NICOLET iS10. A total of 64 scans were collected over a range of 4000 to 400 cm^{-1} with a resolution of 0.2 cm^{-1} for each sample.

2.3 Property evaluations

2.3.1 Dynamic vapor sorption (DVS). DVS experiments were carried out on an SMS DVS instrument (Surface Measurement Systems, UK). Each well-sieved sample (75–150 μm) was initially dried for several hours under a stream of nitrogen to establish the equilibrium dry mass. Then, the relative humidity (RH) was varied over a cycle of 0%–95%–0% in 10% RH increments. The temperature was maintained at a constant value of 25 ± 0.1 °C. The sorption/desorption isotherms were calculated from the equilibrium mass values. Each sample was checked after the DVS experiments by PXRD to detect potential phase changes.

2.3.2 Stability test. Powders of all samples were sieved with controlled particle sizes in the 75–150 μm range. The physical stability of the cocrystal was investigated under 40 °C/75% RH, and that of the coamorphous form was evaluated under 40 °C/75% RH and 25 °C/60% RH conditions, respectively. PXRD was utilized to monitor possible phase changes after 1, 2, 3 and 6 months.

2.3.3 Powder compaction experiment. The powder samples were sieved to control the particle sizes in the range of 75–150 μm, and placed at room temperature for 48 h to eliminate stress. About 50 mg of powder sample was poured into a 5 mm cylindrical mould and pressed through a tablet press machine (Specac GS01190, NY) over a compaction pressure range from 100 to 350 MPa to obtain smooth and flat tablets, which were placed under ambient conditions for 24 h to relieve stress. The diameter D and thickness t of each tablet were measured with a vernier caliper, and then the hardness F of each tablet was tested with a smart tablet hardness analyzer (YD-20KZ, TDTF, China). The tensile strength of each tablet was calculated according to eqn (3):

$$\sigma = \frac{2F}{\pi D t} \quad (3)$$

The tabletability profiles were obtained by plotting the tensile strength as a function of compaction pressure. Three groups (n = 3) were tested in parallel for each experiment to assess standard deviations. PXRD tests were performed on the 350 MPa samples to determine whether any pressure-induced phase transformation had occurred. Environmental conditions were 20–30% RH and 20–25 °C throughout the compaction study.

2.3.4 Dissolution experiment. The powdered samples were ground and then sieved to obtain a 75–150 μm fraction. In a typical experiment, an appropriate amount of the powdered sample (100 mg of GTB, 113.2 mg of DAS·H$_2$O, 221.3 mg of **GTB-DAS·2H$_2$O** or 209.2 mg of **GTB-DAS CM**) was added to a flask containing 30 mL of water containing 5% (v/v) Tween 80. The resulting suspension was stirred at 37 °C and 50 rpm. An aliquot of the slurry was withdrawn and filtered at each predetermined time interval. The filtrate was appropriately diluted and analysed by HPLC to quantify the concentration of GTB and DAS. The dissolution experiments were carried out in triplicate (n = 3) to evaluate standard deviations. After the dissolution experiments, the pH values of the media were measured and the remaining solids were collected and tested by PXRD.

2.3.5 High-performance liquid chromatography (HPLC) assay. HPLC analysis was conducted on a Shimadzu LC-2030C

3D Plus HPLC system with UV detection wavelengths of 254 nm (for GTB) and 322 nm (for DAS) using a C18 column (Inertsil ODS-3, 5 μm × 4.6 mm × 150 mm column, GL Sciences Inc., Japan). The column temperature was set at 35 °C and the injection volume was set as 10 μL. The mobile phase consisted of a mixture of acetonitrile and aqueous phosphoric acid solution containing 0.1% triethylamine (pH 2.4). The gradient elution was used with the flow rate of 1 mL min^{-1}. It was started with 16% (v/v) acetonitrile (3 min), followed by an increase to 60% (v/v) acetonitrile (9.5 min), reversed at 60% (v/v) acetonitrile (14.5 min), and then returned to 16% (v/v) acetonitrile (16.5 min).

3. Results and discussion

3.1 Sample preparation

The cocrystal hydrate **GTB-DAS·2H$_2$O** was discovered by liquid-assisted grinding or rotary evaporation, and the phase-pure bulk sample of it was prepared by the slurry technique. According to variable-temperature PXRD and thermal analyses, it was found that **GTB-DAS·2H$_2$O** converts into an anhydrous **GTB-DAS** by heating to 120 °C to remove water molecules from the lattice. However, no bulk samples of the anhydrate were obtained as it quickly converts back to **GTB-DAS·2H$_2$O** under ambient conditions. Good-quality single crystals of **GTB-DAS·2H$_2$O** were successfully harvested by the evaporation of the methanol solution saturated with **GTB-DAS·2H$_2$O** at room temperature. In contrast, slow evaporation of the methanol–water (with 1 : 1 volume ratio) solution of an equimolar mixture of GTB and DAS·H$_2$O at 4 °C resulted in single crystals of **GTB-DAS·2MeOH**, which were serendipitously contaminated by a few single crystals of **GTB-DAS**. Unfortunately, the single crystals of **GTB-DAS** could not be reproduced afterwards.

The experimental technique used in this work to attain amorphous and coamorphous samples was ball milling. Milling of an equimolar mixture of GTB and DAS·H$_2$O for 180 min resulted in the complete amorphization of the sample and the formation of a coamorphous mixture (**GTB-DAS CM**). Similar milling experiments performed for individual GTB and DAS·H$_2$O also led to the conversion of the crystalline materials into amorphous forms (designated here as GTB AM and DAS AM). It is noteworthy that GTB AM only remains in its amorphous state for a few days due to its high crystallization tendency under ambient conditions.

3.2 PXRD and ^{1}H NMR analysis

PXRD and ^{1}H NMR analysis were utilized to characterize the powdered sample of **GTB-DAS·2H$_2$O**. The presence of new diffraction peaks and the absence of characteristic peaks of the individual components on PXRD patterns prove that a new crystalline form was produced (Fig. 1). The recorded pattern of **GTB-DAS·2H$_2$O** matches well with the simulated PXRD pattern calculated from the single-crystal structure, indicating the phase purity and homogeneity of the bulk sample (Fig. 1). The PXRD patterns of GTB AM, DAS AM, and **GTB-DAS CM** show

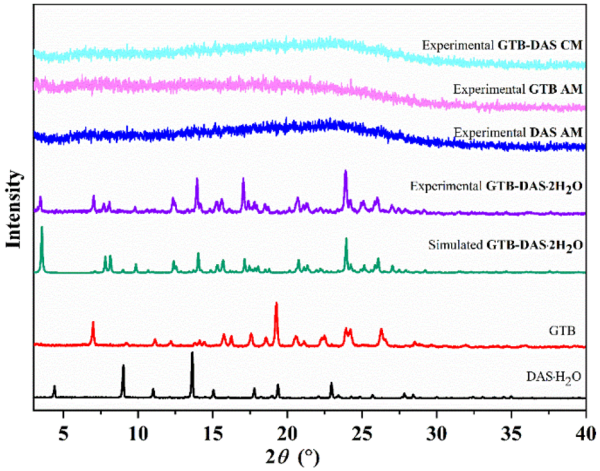

Fig. 1 PXRD patterns of **GTB-DAS·2H$_2$O** and starting components, as well as **GTB-DAS CM**, GTB AM and DAS AM.

typical halos without any signs of crystalline peaks, which are clear characteristics of an amorphous system (Fig. 1).[28] ^{1}H NMR analysis further confirmed the chemical components and stoichiometric ratio of **GTB-DAS·2H$_2$O** (Fig. S1†). The spectra exhibit chemical shifts of GTB and DAS without any peaks of impurity. ^{1}H NMR chemical shift assignments of each chemical component are as follows: peaks of GTB (ppm), δ 9.58 (s, 1H), 8.50 (s, 1H), 8.13 (dd, J = 6.9, 2.7 Hz, 1H), 7.84–7.75 (m, 2H), 7.46 (t, J = 9.1 Hz, 1H), 7.21 (s, 1H), 4.19 (t, J = 6.4 Hz, 2H), 3.94 (s, 3H), 3.59 (t, J = 4.6 Hz, 4H), 2.41 (s, 6H), 2.01 (p, J = 6.7 Hz, 2H);[29] peaks of DAS (ppm), δ 11.50 (s, 1H), 9.90 (s, 1H), 8.23 (s, 1H), 7.41 (dd, J = 7.5, 1.9 Hz, 1H), 7.35–7.19 (m, 2H), 6.05 (s, 1H), 4.48 (t, J = 5.4 Hz, 1H), 3.53 (dt, J = 12.4, 6.1 Hz, 6H), 2.50–2.39 (m, 9H), 2.24 (s, 3H).[30] The combination of PXRD and ^{1}H NMR results indicate the cocrystalline nature of this new crystalline form. By integrating characteristic proton signals of individual components in the ^{1}H NMR spectra, **GTB-DAS·2H$_2$O** shows a 1 : 1 stoichiometric ratio of GTB and DAS.

3.3 Thermal analysis

Thermal analysis was then carried out by TG and DSC measurements (Fig. 2). PXRD was employed to monitor possible phase transitions along with heating (Fig. S2 and S3†). The TG-DSC curve of GTB shows that it is a solvent-free form with a melting endothermic peak at 196.3 °C (Fig. 2a). The TG curve of DAS·H$_2$O exhibits a weight loss of 3.5% corresponding to the loss of the crystalline water (calcd 3.6%). The DSC curve of DAS·H$_2$O shows an endothermic peak at 108.1 °C corresponding to the dehydration process, and an endothermic peak at 288.5 °C attributed to the melting and decomposition process (Fig. 2b).

The TG curve of **GTB-DAS·2H$_2$O** shows a weight loss of 3.6% below 100 °C, corresponding to the loss of two water molecules from the lattice (calc. 3.7%) (Fig. 2c). The DSC curve of **GTB-DAS·2H$_2$O** demonstrates three endothermic peaks at 87.3 °C, 148.4 °C and 190.7 °C as well as one exothermic peak

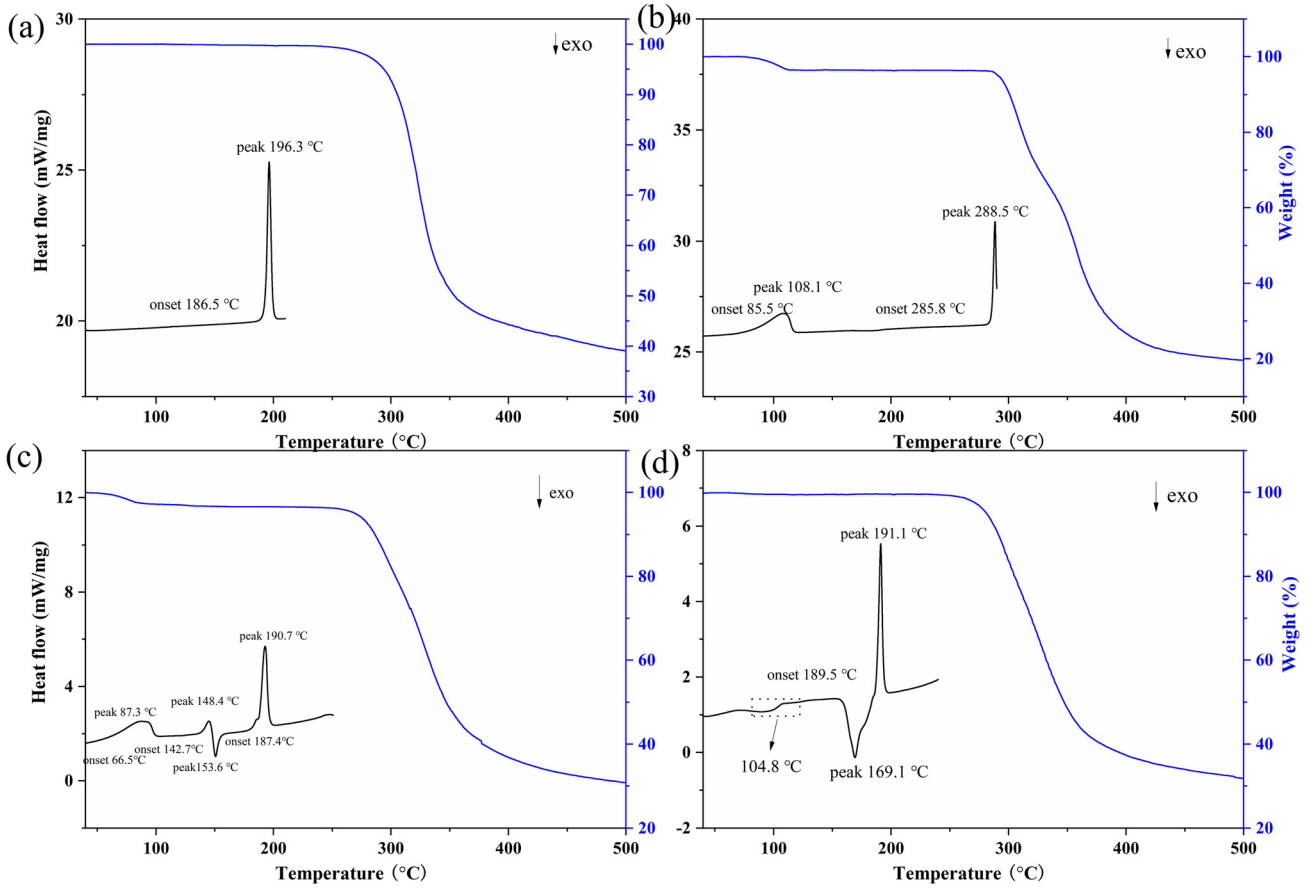

Fig. 2 TG and DSC thermograms of (a) GTB, (b) DAS·H_2O, (c) **GTB-DAS·2H_2O** and (d) **GTB-DAS CM**.

at 153.6 °C (Fig. 2c), which corresponds to multi-step phase transformations, and were further confirmed by variable temperature PXRD analysis (Fig. S2†). The first endothermic peak at 87.3 °C can be attributed to the loss of crystalline water, leading to the formation of anhydrous **GTB-DAS**, which is consistent with the phase change between 100 and 120 °C in variable temperature PXRD diffractograms. The second endothermic peak at 148.4 °C is followed by the exothermic peak at 153.6 °C, corresponding to the phase transition from **GTB-DAS** to a physical mixture of GTB and DAS. It is also proved by the change of PXRD patterns from 140 to 145 °C. The last endothermic peak at 190.7 °C points to the melting of GTB and only DAS being left, which is further confirmed from the change of PXRD diffractograms in the temperature range of 180–200 °C. Finally, the crystalline phase of DAS stays until the temperature cooled back to 25 °C.

Three distinct phase transitions were observed on the DSC profile of **GTB-DAS CM**, namely, a glass transition at 104.8 °C, which is followed by an exothermal crystallization event at 169.1 °C, and an endothermic melting event at 191.1 °C (Fig. 2d). The appearance of a single T_g for the coamorphous mixture indicates the formation of a homogeneous phase rather than a physical mixture of amorphous GTB and DAS. The PXRD analysis was performed to identify the phase composition of the material crystallized at 169.1 °C, and the result shows that it was a physical mixture of crystalline GTB and DAS. Then the endothermic event occurring at 191.1 °C could be attributed to the melting of GTB.

Furthermore, MDSC was carried out for **GTB-DAS CM** with amorphous GTB and DAS as controls (Fig. S4–S6†). The MDSC thermograms demonstrate T_g values of 68.4 ± 0.1 °C and 134.1 ± 0.1 °C for single amorphous GTB and DAS, respectively. For **GTB-DAS CM**, a single T_g value of 100.4 ± 0.1 °C was determined, which is between those of the single amorphous drugs and is close to the conventional DSC data of **GTB-DAS CM**. The theoretical T_g value of the coamorphous system can be calculated using the Gordon–Taylor formula, and the strength of the interaction between components can be judged by comparing with the measured T_g.[31] The experimental T_g value (100.4 ± 0.1 °C) of **GTB-DAS CM** exhibits a slight positive deviation from the theoretical T_g value (98.7 °C), indicating that no significant molecular interactions exist between GTB and DAS in the coamorphous state.[32]

3.4 Crystal structure and the Hirshfeld surface analysis

Single crystals of **GTB-DAS·2H_2O**, **GTB-DAS·2MeOH** and **GTB-DAS** were determined and resolved. Table 1 presents the collected crystallographic data, and Table 2 lists the hydrogen bonding geometry parameters. All three cocrystals belong to the monoclinic $P2_1/n$ space group with similar unit cells

Table 1 Crystallographic data of **GTB-DAS·2H$_2$O**, **GTB-DAS·2MeOH** and **GTB-DAS**

Compound	**GTB-DAS·2H$_2$O**	**GTB-DAS·2MeOH**	**GTB-DAS**
Chem. formula	$C_{44}H_{54}Cl_2FN_{11}O_7S$	$C_{46}H_{58}Cl_2FN_{11}O_7S$	$C_{44}H_{50}Cl_2FN_{11}O_5S$
Formula wt.	970.94	998.99	934.91
Temp (K)	295(10)	150(10)	295(10)
Cryst. syst.	Monoclinic	Monoclinic	Monoclinic
Space group	$P2_1/n$	$P2_1/n$	$P2_1/n$
Crystal size (mm^3)	0.1 × 0.08 × 0.06	0.1 × 0.05 × 0.05	0.1 × 0.06 × 0.04
a (Å)	25.0616(14)	24.6417(3)	24.0553(11)
b (Å)	8.5546(9)	9.01060(10)	8.2878(4)
c (Å)	22.8246(13)	22.0764(3)	22.7287(7)
α (°)	90	90	90
β (°)	97.457(5)	101.2970(10)	91.233(3)
γ (°)	90	90	90
V (Å^3)	4852.0(6)	4806.79(10)	4530.3(3)
Z	4	4	4
Density (g cm^{-3})	1.325	1.380	1.371
2θ range	7.812–161.092	7.316–159.386	7.352–159.366
F (000)	2040	2104	1960
Index ranges	$-31 \le h \le 31$ $-10 \le h \le 8$ $-28 \le h \le 29$	$-31 \le h \le 30$ $-8 \le h \le 11$ $-28 \le h \le 25$	$-29 \le h \le 30$ $-8 \le k \le 10$ $-28 \le l \le 22$
No. of reflns	10 082	10 229	6839
No. of unique reflns	6266	9014	9414
No. of params	794	725	662
R_{1all}, R_{1obs} [a]	0.1221, 0.0826	0.0498, 0.0447	0.0904, 0.0659
wR_{2all}, wR_{2obs} [b]	0.2527, 0.2217	0.1176, 0.1140	0.1669, 0.1513
GOF	1.035	1.055	1.040
CCDC no.	2 330 839	2 330 840	2 330 841

[a] $R_1 = \sum||F_o| - |F_c||/\sum|F_o|$. [b] $wR_2 = [\sum[w(F_o^2 - F_c^2)^2]/\sum w(F_o^2)^2]^{1/2}$, $w = 1/[\sigma^2(F_o)^2 + (aP)^2 + bP]$, where $P = [(F_o^2) + 2F_c^2]/3$.

Table 2 Selected hydrogen bonding distances and angles of **GTB-DAS·2H$_2$O**, **GTB-DAS·2MeOH** and **GTB-DAS**

Hydrogen bond	H···A (Å)	D···A (Å)	∠D–H···A (°)	Symmetry code
GTB-DAS·2H$_2$O				
N4–H4···N6	2.116	2.976	179.8	$-x+2, -y+1, -z+1$
N8–H8A···O1	1.996	2.817	159.5	$-x+2, y-1/2, -z+1/2$
O4–H4A···N2	2.119	2.756	134.8	$-x+1, -y+1, -z+1$
O4–H4A···N2A	2.235	2.864	133.8	$-x+1, -y+1, z+1$
GTB-DAS·2MeOH				
N9–H9···N10	2.056	2.913	174.3	$-x, -+2, -z+1$
N11–H11···O5	1.985	2.834	168.8	$-x, y+1/2, -z+3/2$
N11–H11A···O5	1.990	2.834	166.8	$-x, y+1/2, -z+3/2$
N4–H4A···O6	2.174	2.983	156.6	
N4–H4B···O6	2.195	2.983	152.3	
O4–H4···N1	2.164	2.864	143.3	
O6–H6···O7	1.868	2.685	174.6	
O7–H7···N2	1.915	2.722	167.9	$-x+1, -y+1, -z+1$
O4A–H4A···N1	2.219	2.954	149.3	
GTB-DAS				
O4–H4···O1	1.961	2.779	175.0	$-x+1, -y+1, -z+1$
N9–H9···N10	2.109	2.959	169.3	$-x+2, -y+2, -z+1$
N4–H4A···O4	2.486	2.874	157.1	$x, -y+3/2, z+1/2$
N11–H11–O5	1.976	2.844	151.1	$-x+2, y+1/2, -z+3/2$

(Table 1). The asymmetric units of **GTB-DAS·2H$_2$O** and **GTB-DAS·2MeOH** consist of one molecule of GTB, one molecule of DAS, and two molecules of water/methanol (Fig. 3a and 4a) while that of **GTB-DAS** contains one molecule each of GTB and DAS (Fig. 5a). In all cocrystals, two DAS molecules pair up through double N–H···N hydrogen bonding interactions of thiazole nitrogen with the amino group at its *ortho* position to form a dimer, which further connects *via* N–H···O hydrogen bonding interactions of the amide group to produce a one-dimensional (1D) DAS chain. Adjacent DAS chains alternately link together with an angle to form a two-dimensional (2D) wavy layer (Fig. 3b, c, 4b, c and 5b, c). GTB molecules in **GTB-DAS·2H$_2$O** and **GTB-DAS·2MeOH** are embedded in the concave of neighbouring DAS layers through weak O4–H4A···N2/N2A (2.756 Å, 134.8°/2.864 Å, 133.8°) and O4–H4A···N1 (2.864 Å, 143.3°) hydrogen bonding interactions, respectively, to generate a three-dimensional (3D) framework containing water/methanol molecules in 1D channels comprised of GBT (Fig. 3df and 4df). In contrast, GTB molecules in **GTB-DAS** insert into the concave of neighbouring DAS layers through relatively strong N4–H4A···O4 and O4–H4···O1 hydrogen bonding interactions to generate a 3D framework without any channels (Fig. 5d–f).

To compare molecular arrangements and noncovalent interactions, in particular, hydrogen bonding interactions before and after cocrystallization, the crystal structure of each parent crystalline drug was analysed from a crystal engineering perspective. GTB molecules of the parent GTB crystal are packed together to generate the 3D structure *via* van der Waals forces rather than hydrogen bonding and π–π interactions, similar to that of cocrystals (Fig. S7†).[33] DAS molecules of the parent DAS crystal form similar dimers, chains, and wavy layer structures through N–H (amine)···N (thiazole) interactions and N–H (amide)···O (carbonyl) interactions, just like that of the

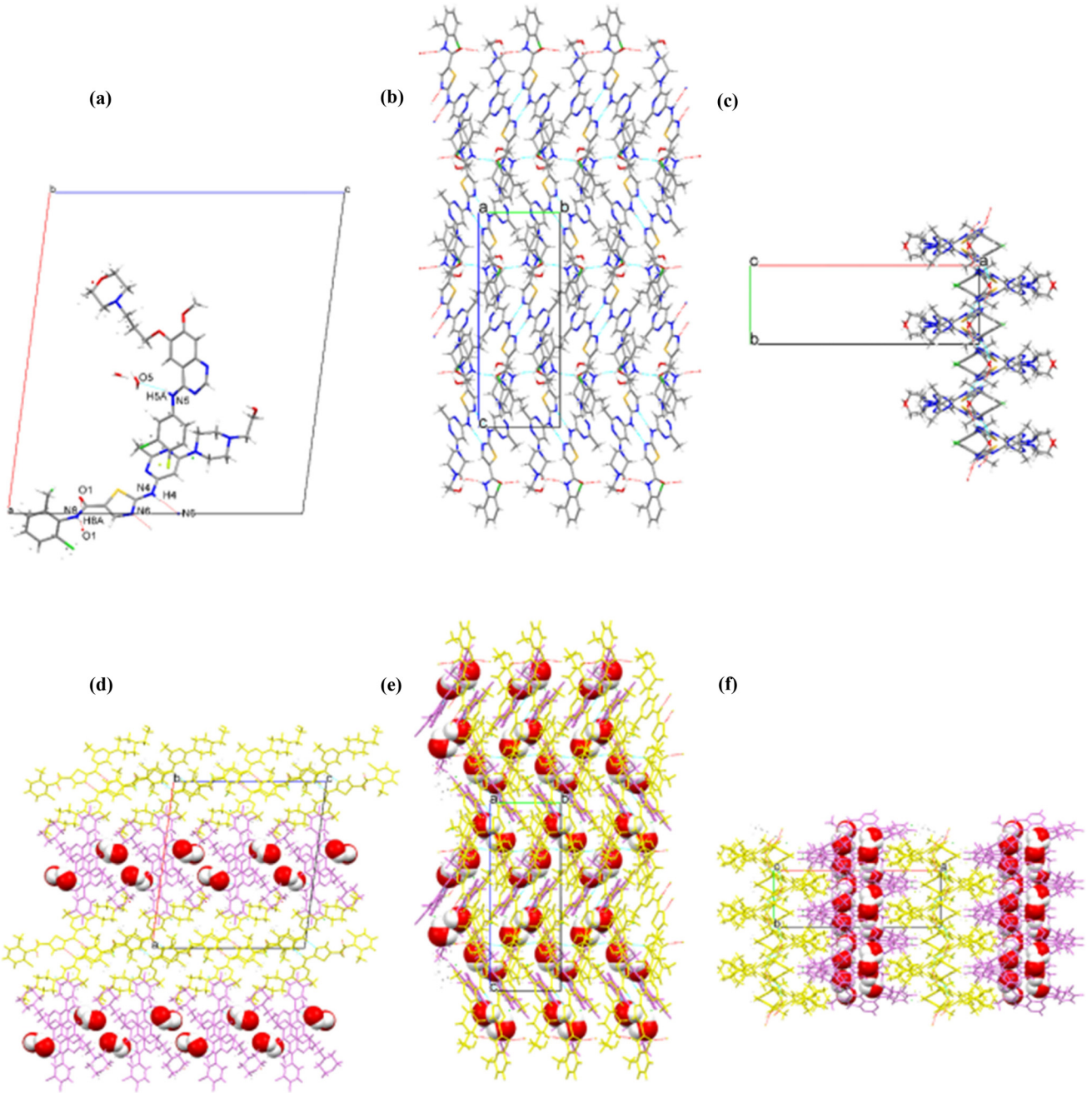

Fig. 3 (a) Asymmetric unit along the *b*-axis. DAS layer packed along (b) the *a*-axis and (c) the *c*-axis. 3D framework packed along (d) the *b*-axis, (e) the *a*-axis and (f) the *c*-axis for **GTB-DAS·2H$_2$O**. Violet molecules correspond to GTB, and yellow molecules correspond to DAS.

cocrystals (Fig. S8†).[34] From crystal structure analysis, we can see that main molecular interactions of each single component are retained after cocrystallization, and GTB and DAS in **GTB-DAS·2H$_2$O** interact with each other *via* van der Waals forces and weak hydrogen bonding interactions. Hirshfeld surface analysis was carried out based on the single-crystal structures to evaluate in detail the intermolecular interactions in both qualitative and quantitative terms.[35] The relative contributions of various intermolecular contacts are shown in Fig. 6. The 2D fingerprint plots of dominant intermolecular interactions are graphed in Fig. S9.† These confirm that the most prominent contributions for **GTB-DAS·2H$_2$O**, **GTB-DAS·2MeOH** and **GTB-DAS** are provided by H···H corresponding to van der Waals forces, with percentages of 50.90%, 46.00% and 55.40%, respectively.

3.5 FTIR analysis

FTIR spectroscopy was carried out in order to gain additional insights into possible molecular level interactions between GTB and DAS in the cocrystalline and coamorphous forms

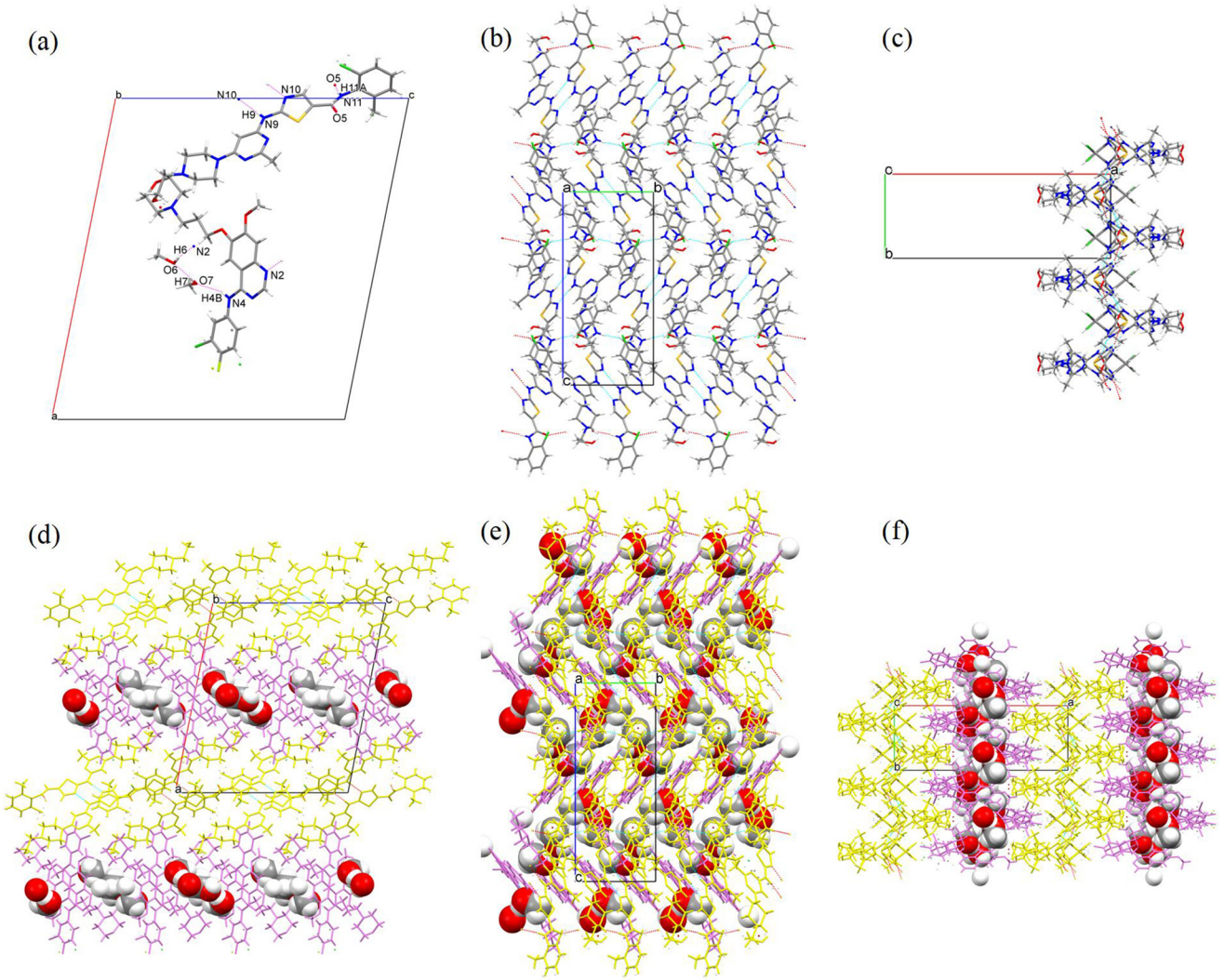

Fig. 4 (a) Asymmetric unit along the *b*-axis. DAS layer packed along (b) the *a*-axis and (c) the *c*-axis. 3D framework packed along (d) the *b*-axis, (e) the *a*-axis and (f) the *c*-axis for **GTB-DAS·2MeOH**. Violet molecules correspond to GTB, and yellow molecules correspond to DAS.

(Fig. 7). The spectral analysis was focused on the regions of 1650–1600 cm^{-1} (C═O/N stretching) and 1600–1550 cm^{-1} (aromatic C═C stretching), since significant peak shifts related to possible hydrogen bonding and π–π interactions between GTB and DAS upon cocrystallization and coamorphization could be detected there. Crystalline GTB exhibits characteristic peaks at 1624 cm^{-1} (C═N stretching) and 1582 cm^{-1} (aromatic C═C stretching), while crystalline DAS exhibits main bands at 1622 cm^{-1} (C═O stretching) and 1583 cm^{-1} (aromatic C═C stretching). The FTIR spectrum of the physical mixture of GTB and DAS (GTB-DAS PM) contains the superimposed spectra of each component.

In the FTIR spectra of **GTB-DAS·2H$_2$O**, no considerable shifts of absorption bands associated with H-bonds (C═N and C═O stretching) and π–π interactions (aromatic C═C stretching) were observed, confirming the absence of strong molecular interactions between GTB and DAS. This agrees well with the crystal structure and Hirshfeld surface analyses that the most prominent intermolecular interactions between GTB and DAS of cocrystals are van der Waals forces. The FTIR spectra of **GTB-DAS CM** appeared to be comparable with those of the cocrystals in terms of most peak positions, except that the peaks are broadened with lower intensity, indicating amorphous nature. This suggests that the molecular arrangement of **GTB-DAS CM** is fairly similar to that of the cocrystalline counterpart, with no significant molecular interactions between GTB and DAS. This is also consistent with the conclusion made based on the very small difference between theoretically and experimentally determined T_g values of **GTB-DAS CM**.

3.6 Dynamic vapor sorption (DVS) and stability test

Cocrystallization and coamorphization of certain drug combinations can only be practically useful if their hygroscopicity and physical stability are confirmed. The hygroscopicity of GTB, DAS·H$_2$O, **GTB-DAS·2H$_2$O** and **GTB-DAS CM** were studied

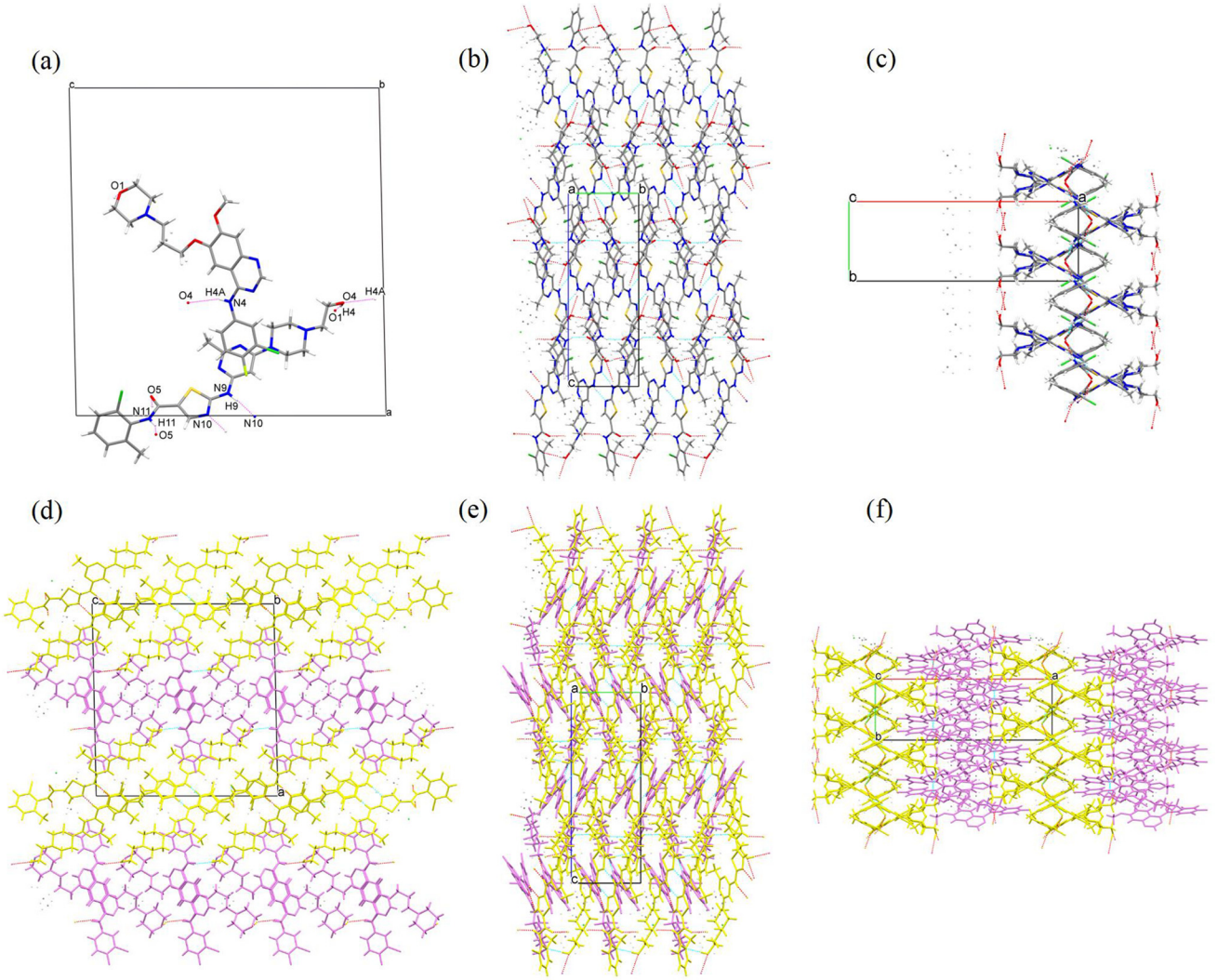

Fig. 5 (a) Asymmetric unit along the *b*-axis. DAS layer packed along (b) the *a*-axis and (c) the *c*-axis. 3D framework packed along (d) the *b*-axis, (e) the *a*-axis and (f) the *c*-axis for **GTB-DAS**. Violet molecules correspond to GTB, and yellow molecules correspond to DAS.

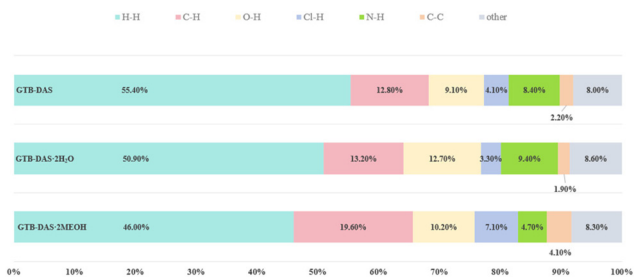

Fig. 6 The percentage contributions to the Hirshfeld surface area of various intermolecular contacts of **GTB-DAS**, **GTB-DAS·2H$_2$O** and **GTB-DAS·2MeOH**.

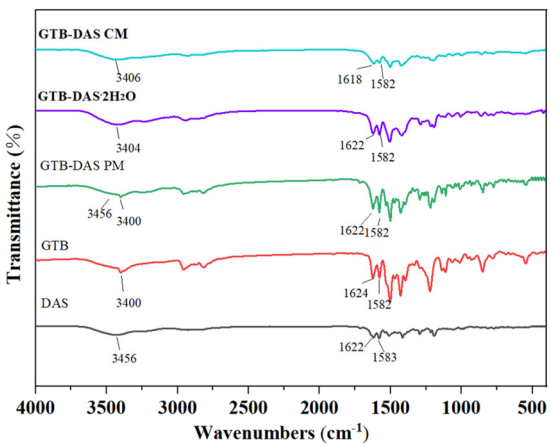

Fig. 7 FTIR spectra of GTB, DAS, GTB-DAS PM, **GTB-DAS·2H$_2$O** and **GTB-DAS CM**.

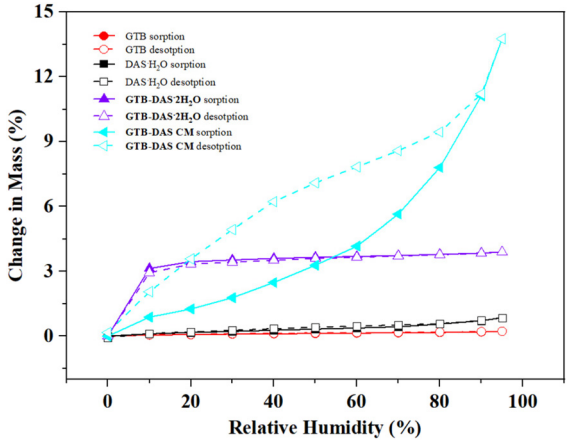

Fig. 8 Water sorption/desorption isotherms of GTB, DAS·H_2O, **GTB-DAS·2H_2O** and **GTB-DAS CM**.

by DVS measurements at 25 °C (Fig. 8). Possible phase transitions associated with DVS experiments were monitored by PXRD measurements (Fig. S10†).

GTB and DAS·H_2O exhibit simple sorption/desorption behaviour showing 0.17% and 0.74% mass change as the humidity increased from 10% to 95%. It is worth noting that the crystalline water of DAS·H_2O is so stable that it remains even under 0% RH.

During the initial drying stage, **GTB-DAS·2H_2O** lost approximately two molecules of water (with 3.49% mass change) to form **GTB-DAS** under 0% RH. Then **GTB-DAS** absorbed moisture (with 3.31% mass change) and was converted back into **GTB-DAS·2H_2O** as the humidity increased to 10%, and further absorbed a little more moisture on the surface as the humidity increased from 10% to 95% (with total 4.12% mass change). During the desorption process, **GTB-DAS·2H_2O** reversably lost the water on the surface as the humidity decreased from 95% to 10%, and then it totally lost the crystalline water and converted into anhydrous **GTB-DAS** at 0% RH. The above results imply a humidity-induced transition between the hydrate and anhydrous form. **GTB-DAS** can be formed under 0% RH, while **GTB-DAS·2H_2O** is the stable form across a wide range of 10%–95% RH. However, the PXRD analysis of the sample equilibrating under 0% RH and 95% RH both revealed the crystal phase of **GTB-DAS·2H_2O**. This can be explained by the **GTB-DAS** that formed under 0% RH being converted back to **GTB-DAS·2H_2O** when the sample was taken out for PXRD measurement. This is consistent with the fact that the bulk sample of **GTB-DAS** cannot be prepared by dehydration of **GTB-DAS·2H_2O** through heating due to the rapid hydration process of **GTB-DAS** under ambient conditions.

In contrast, **GTB-DAS CM** exhibits simple sorption/desorption behaviour, showing no evidence of phase transitions (Fig. 8). It lost the adsorbed water molecules (with 2.40% mass change) during the initial drying stage. Then it moderately absorbed moisture below 60% RH (with 4.17% mass change), while it rapidly absorbed water above 60% RH and totally absorbed 13.75% of water under 95% RH. During the desorption process, **GTB-DAS CM** gradually lost the absorbed water with a hysteresis gap. The PXRD patterns of **GTB-DAS CM** under 0% RH and 95% RH confirmed that the amorphous state remains throughout the 0%–95% RH range (Fig. S10†), showing stabilization against moisture-induced crystallization of this formulation.

GTB-DAS·2H_2O and **GTB-DAS CM** were stored under 40 °C/75% RH conditions and then PXRD measurements were conducted to evaluate their physical stability with time intervals of 1, 2, 3 and 6 months (Fig. S11†). **GTB-DAS·2H_2O** retains its original phase over the period of storage, while **GTB-DAS CM** undergoes crystallization with distinctive peaks belonging to crystalline GTB and DAS in the PXRD diffractograms within 2 months. Furthermore, the stability of **GTB-DAS CM** was evaluated under 25 °C/60% RH conditions for 6 months. The result shows that **GTB-DAS CM** stays amorphous over the whole period, indicated by the appearance of a halo in the PXRD diffractogram.

3.7 Tabletability property

Tabletability refers to the ability of a powdered drug to be transformed into a tablet with a specific tensile strength over a certain range of compaction pressures.[36] The change of solid forms can modulate the tabletability property and therefore the manufacturability of a given drug.[37] In this study, the tabletability values of GTB, DAS·H_2O, **GTB-DAS·2H_2O** and **GTB-DAS CM** were determined under compaction pressures from 100 to 350 MPa. The tabletability profiles are shown in Fig. 9. The tablet tensile strengths of crystalline GTB, DAS·H_2O and **GTB-DAS·2H_2O** increase with the increase of compaction pressure from 100 to 250 MPa. However, a further increase in the compaction pressure results in a decline in the tensile strength, which is known as overcompaction.[38] The tabletability of crystalline powders is relative to the molecular arrangements and packing modes of the crystals. As **GTB-DAS·2H_2O**

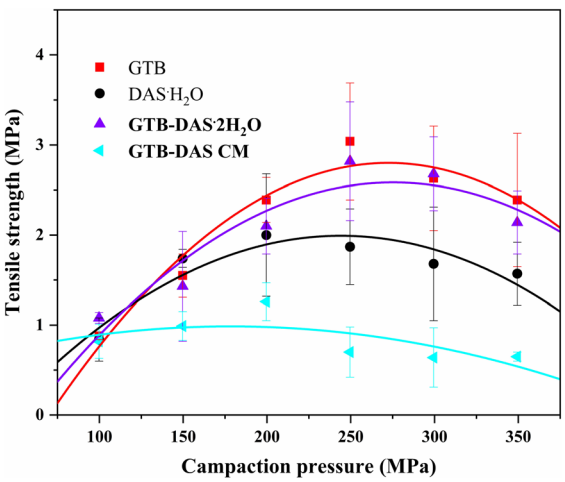

Fig. 9 Tabletability profiles of GTB, DAS·H_2O, **GTB-DAS·2H_2O** and **GTB-DAS CM**.

maintains main molecular packing modes of both pure GTB and DAS·H_2O, the tablet tensile strength of the **GTB-DAS·2H_2O** lies between that of the two individual crystalline components in the compaction pressure range of 100 to 350 MPa.

The tablet tensile strength of **GTB-DAS CM** is much lower than that of **GTB-DAS·2H_2O** under the same compaction pressures due to the long-range disordered structure of the amorphous material. **GTB-DAS·2H_2O** and **GTB-DAS CM** reach the maximum tensile strengths of 2.82 and 1.26 MPa, respectively. A threshold tensile strength of 2 MPa, which ensures integrity of a pharmaceutical tablet, has been achieved by **GTB-DAS·2H_2O**.[39] The superior tabletability of **GTB-DAS·2H_2O** may be attributed to the alternately layered structures of GTB and DAS as well as the existence of water molecules in the lattice, leading to significant plastic deformation under compaction. After experiments, the powdered samples were collected and determined by PXRD tests. The results reveal that there was no stress-induced phase transition during the compaction process (Fig. S12†).

3.8 Dissolution study

The powder dissolution experiments were carried out in Tween 80 aqueous solution (5% v/v)[40,41] for **GTB-DAS·2H_2O** and **GTB-DAS CM** under non-sink conditions with crystalline GTB and DAS·H_2O as controls.[42] The 8 h dissolution profiles are shown in Fig. 10. The time to attain the maximum concentration (T_{max}), the maximum concentration (C_{max}), and the area under the curve (AUC) of GTB and DAS obtained from the concentration–time profiles are summarized in Table 3. After the dissolution experiments, the undissolved solids were isolated by filtration and identified by PXRD tests (Fig. S13†). Crystalline GTB reached the C_{max} value (664.64 ± 0.24 μg mL^{-1}) within the first 20 min of the dissolution experiment, followed by gradual decline due to recrystallization of the more stable but less soluble hydrated form of GTB (identified as GTB·3H_2O as shown by PXRD). The dissolution profile of crystalline DAS·H_2O shows that the parent drug dissolved slowly, reaching a concentration plateau with the C_{max} value of 150.70 ± 0.17 μg mL^{-1}. There is a 4.4-times solubility difference between pure GTB and DAS·H_2O, suggesting potential compatibility issues between the two drugs.

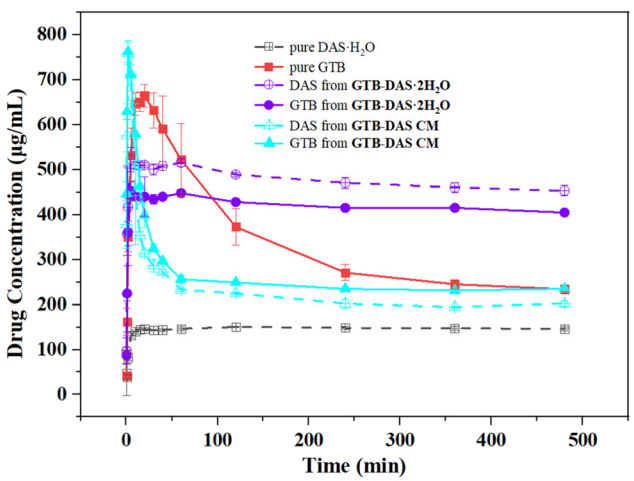

Fig. 10 Dissolution profiles of GTB and DAS from pure GTB, DAS·H_2O, **GTB-DAS·2H_2O** and **GTB-DAS CM**.

GTB-DAS·2H_2O exhibits synchronized release of the two drugs with improved dissolution performance. The dissolution behaviour of GTB and DAS can be described as the "spring and hover" model.[43] Both GTB and DAS dissolved much faster and generated supersaturation almost instantly (within 5 min), with the C_{max} values of 440.52 ± 0.51 μg mL^{-1} and 509.46 ± 0.12 μg mL^{-1}, respectively. After reaching C_{max}, the GTB and DAS concentration slightly dropped within 8 h. Although **GTB-DAS·2H_2O** yielded a lower C_{max} value of GTB as compared to free GTB, the dissolution of GTB and DAS was effectively improved by contributing to a prolonged supersaturation. The PXRD pattern of the undissolved residue from the dissolution experiment revealed characteristic peaks of **GTB-DAS·2H_2O**, which is consistent with the "hover" effect of drug concentrations. Synchronized drug release can be attributed to the superior physical stability of the cocrystal during dissolution and is a desired attribute in the oral administration of combinational therapy.

GTB-DAS CM also shows similar dissolution profiles for GTB and DAS, releasing both drugs in a synchronized manner. It exhibits the shortest T_{max} and the highest C_{max} for GTB (2 min, 762.31 ± 0.24 μg mL^{-1}) and DAS (2 min, 758.33 ± 0.22 μg mL^{-1}), yielding the "spring up" effect. The C_{max} values of GTB and DAS released from the coamorphous form were found to increase by a factor of 1.1 and 5.0 compared to crystalline GTB and DAS·H_2O. The improvement of the dissolution of **GTB-DAS CM** can be attributed to a high Gibbs free energy of the coamorphous state since less energy is required to dissolve molecules from a disordered solid compared with a crystalline material. However, the elevated GTB and DAS concentrations of **GTB-DAS CM** were not sustained and decreased rapidly over time as it is thermodynamically unstable and tends to crystallize into thermodynamically stable forms during dissolution, resulting in the "spring down" stage. This is in line with the PXRD analysis of the undissolved solids collected after the dissolution experiment, which revealed characteristic peaks of crystalline GTB·3H_2O and DAS·H_2O.

The dissolution performance was also evaluated in terms of AUC values of the dissolution curves (Table 3). Compared to the AUC values of GTB ((160.16 ± 12.23) × 10^3 μg min mL^{-1}) and DAS ((70.65 ± 0.12) × 10^3 μg min mL^{-1}) free drugs, those values of **GTB-DAS·2H_2O** were increased by 1.3 and 3.2-fold, respectively. In contrast, **GTB-DAS CM** exhibits much lower AUC values of GTB and DAS than cocrystalline forms, though the C_{max} values appeared to be even higher than those of the cocrystal. The observed variation in the AUC values of the cocrystalline and coamorphous forms can be attributed to the differences in the recrystallization rates of the materials during dissolution. Thus, the cocrystal exhibits significant dissolution advantage over the coamorphous form due to its stronger physical stability and longer-lasting supersaturation as revealed in this work.

Table 3 The time to attain the maximum concentration (t_{max}), the maximum concentration (C_{max}), and the area under the curve ($AUC_{0\text{-}8h}$) of GTB and DAS

Sample	$t_{max,\ GTB}$ (min)	$C_{max,\ GTB}$ (μg mL^{-1})	$AUC_{0\text{-}8h,\ GTB}$ (μg min mL^{-1})	$t_{max,\ DAS}$ (min)	$C_{max,\ DAS}$ (μg mL^{-1})	$AUC_{0\text{-}8h,\ DAS}$ (μg min mL^{-1})
GTB	20	664.64 ± 0.24	(160.16 ± 12.2) × 10^3	—	—	—
DAS·H_2O	—	—	—	120	150.70 ± 0.17	(70.65 ± 0.12) × 10^3
GTB-DAS·2H_2O	20	440.52 ± 0.51	(201.89 ± 0.14) × 10^3	5	509.46 ± 0.12	(228.65 ± 1.02) × 10^3
GTB-DAS CM	2	762.31 ± 0.24	(148.29 ± 1.54) × 10^3	2	758.33 ± 0.22	(118.10 ± 1.85) × 10^3

4. Conclusions

Herein, both cocrystallization and coamorphization techniques were applied to two poorly soluble drugs with synergistic antitumor activity, *i.e.* GTB and DAS, with the intention to optimize the performance of hybrid drugs for the exertion of their synergistic effect. One cocrystal hydrate **GTB-DAS·2H_2O** (1 : 1 : 2) was prepared by both liquid-assisted grinding and solvent-based methods (*i.e.* evaporation crystallization and slurry) while one coamorphous form **GTB-DAS CM** (1 : 1) was obtained by the neat milling technique. Although anhydrous **GTB-DAS** can be formed by removal of the crystalline water of **GTB-DAS·2H_2O** by heating to 120 °C or drying under 0% RH, it quickly converts back into the cocrystal hydrate under ambient conditions. Therefore, the bulk sample of **GTB-DAS** cannot be obtained due to its extreme instability. The obtained bulk samples of **GTB-DAS·2H_2O** and **GTB-DAS CM** were fully characterized by XRD, ^{1}H NMR, thermal analysis, FTIR and DVS measurements. Crystal structural and Hirshfeld surface analyses demonstrate that main molecular packing and interactions of individual crystalline components were retained in **GTB-DAS·2H_2O**, and that the GTB and DAS in cocrystals mainly interact with each other *via* van der Waals forces. The amorphization of **GTB-DAS CM** was confirmed by a halo pattern in PXRD measurements and a single glass transition event in the DSC and MDSC curves. The stability, tabletability and dissolution performances of **GTB-DAS·2H_2O** and **GTB-DAS CM** were then systematically evaluated. Overall, **GTB-DAS·2H_2O** shows superior stability and tabletability performance, and synchronized drug release with improved dissolution behaviour, making it a more promising and reliable solid form for the development of combinational therapy.

Author contributions

Xian-Bi Shi: conceptualization, data curation, methodology, validation, investigation, visualization, and writing – original draft; Zhi-Qing Wang: data curation and visualization; Hui-Tian Li: data curation and visualization; Xia-Lin Dai: computational studies; Yong-Liang Huang: refinement of single-crystal structures; Xiang-Tian Long: conceptualization, resources, and writing – review and editing; Jia-Mei Chen: conceptualization, project administration, funding acquisition, resources, and writing – review and editing; Tong-Bu Lu: conceptualization and resources.

Data availability

Crystallographic data have been deposited at the CCDC under 2330839–2330841.† For the ESI† and crystallographic data see **https://doi.org/10.1039/D4PM00237G**.

Conflicts of interest

There are no conflicts to declare.

Acknowledgements

This work was financially supported by the National Natural Science Foundation of China (No. 22271220) and the Graduate Education and Teaching Research and Reform Project of Tianjin University of Technology (No. YBXM2321).

References

1 J. Lehár, A. S. Krueger, W. Avery, A. M. Heilbut, L. M. Johansen, E. R. Price, R. J. Rickles, G. F. Short, J. E. Staunton, X. W. Jin, M. S. Lee, G. R. Zimmermann and A. A. Borisy, *Nat. Biotechnol.*, 2009, **27**, 659–666.
2 P. Das, M. D. Delost, M. H. Qureshi, D. T. Smith and J. T. Njardarson, *J. Med. Chem.*, 2019, **62**, 4265–4311.
3 C. Melikian, T. J. White, A. Vanderplas, C. M. Dezii and E. Chang, *Clin. Ther.*, 2002, **24**, 460–467.
4 K. Jazieh, J. Molina, J. Allred, J. Yin, J. Reid, M. Goetz, V. S. Lim, S. H. Kaufmann and A. Adjei, *Invest. New Drugs*, 2019, **37**, 307–314.
5 C. Borghi and A. F. G. Cicero, *Clin. Drug Invest.*, 2010, **30**, 843–854.
6 D. Desai, J. Wang, H. Wen, X. Li and P. Timmins, *Pharm. Dev. Technol.*, 2013, **18**, 1265–1276.
7 F. Simon, *Nat. Rev. Drug Discovery*, 2006, **5**, 881–882.
8 B. P. Bezerra, D. Pogoda, M. L. Perry, L. Vidal, M. J. Zaworotko and A. P. Ayala, *Cryst. Growth Des.*, 2020, **20**, 4707–4718.
9 K. V. Drozd, A. N. Manin, A. V. Churakov and G. L. Perlovich, *CrystEngComm*, 2017, **19**, 4273–4286.
10 X. Li, X. Liu, J. Song, C. Wang, J. Li, L. Liu, X. He, X. Zhao and C. C. Sun, *Cryst. Growth Des.*, 2021, **21**, 3461–3468.

11 F. Y. Zhou, J. L. Zhou, H. L. Zhang, H. H. Y. Tong, J. J. Nie, L. Li, Y. Y. Zhang, J. Du, A. D. Ma, X. M. Yang and Z. Z. Zhou, *J. Drug Delivery Sci. Technol.*, 2019, **54**, 101244.
12 M. Banerjee, K. Nimkar, S. Naik and V. Patravale, *J. Controlled Release*, 2022, **348**, 456–469.
13 W. X. Wang, F. Liu, J. Y. Li, J. Xue, Y. T. Li and R. M. Liu, *J. Mol. Struct.*, 2021, **1243**, 130729.
14 P. M. Nielsen, D. Grimm, M. Wehland, U. Simonsen and M. Krüger, *Basic Clin. Physiol. Pharmacol.*, 2018, **122**, 9–18.
15 H. Fael and A. L. Demirel, *Int. J. Pharm.*, 2021, **600**, 120448.
16 Y. Shen, M. Aucamp, H. E. Abdelhakim, X. Li, Y. Ghazali and K. Edkins, *RSC Pharm.*, 2024, **1**, 132–140.
17 M. Skotnicki, B. Jadach, A. Skotnicka, B. Milanowski, L. Tajber, M. Pyda and J. Kujawski, *Pharmaceutics*, 2021, **13**, 118.
18 S. K. Wilke, C. J. Benmore, V. Menon, D. Smith, S. R. Byrn and R. Weber, *RSC Pharm.*, 2024, **1**, 121–131.
19 P. Agarwal, D. Svirskis and M. K. Nieuwoudt, *RSC Pharm.*, 2024, **1**, 296–304.
20 S. Saeki, J. Sasaki, J. Morioka, R. Sato, S. Sakata, H. Ichiyasu, K. Fujii, N. Saita and H. Kohrogi, *J. Clin. Oncol.*, 2012, **30**, e18059.
21 S. Nanjo, S. Arai, W. Wang, S. Takeuchi, T. Yamada, A. Hata, N. Katakami, Y. Okada and S. Yano, *Mol. Cancer Ther.*, 2017, **16**, 506–515.
22 C. Zhang, X. Zhao, Z. Wang, T. Gong, H. Zhao, D. Zhang, Y. Niu, X. Li, X. Zhao, G. Li, X. Dong, L. Zhang, C. Liu, J. Xu and B. Yu, *Invest. New Drugs*, 2023, **41**, 438–452.
23 Z. Wang, L. Li, Z. Shao, H. Xie, F. Yang and N. Zhou, *Chin. J. Cell. Mol. Immunol.*, 2016, **32**, 595–599.
24 B. Thibault and B. Jean-Claude, *J. Ovarian Res.*, 2017, **10**, 1–12.
25 D. Nagdiya, M. Kumar, S. Arora, T. Bajaj, S. Kujur, P. Rana, A. Kumar, A. Singh and C. Singh, *OpenNano*, 2023, **14**, 100183.
26 A. Shaik, P. U. Bhagwat, P. Palanisamy, D. Chhabria, P. Dubey, S. Kirubakaran and V. Thiruvenkatam, *CrystEngComm*, 2023, **25**, 2570–2581.
27 G. Sodeifian, R. S. Alwi, F. Razmimanesh and M. Abadian, *J. Mol. Liq.*, 2022, **346**, 117899.
28 R. Shelke, V. Velagacherla and U. Y. Nayak, *Drug Discovery Today: Technol.*, 2024, **29**, 103863.
29 M. Z. Chen, L. Wang, L. H. Zhang, W. F. Li and Y. C. Ding, *Chin. J. Magn. Reson.*, 2017, **28**, 413–418.
30 P. W. Manley, S. W. Cowan-Jacob, G. Fendrich, A. Strauss, N. Vapai, S. Grzesiek and W. Jahnke, *Blood*, 2006, **108**, 747.
31 S. Saboo, U. S. Kestur, D. P. Flaherty and L. S. Taylor, *Mol. Pharmaceutics*, 2020, **17**, 1261–1275.
32 S. Baghel, H. Cathcart and N. J. O'Reilly, *J. Pharm. Sci.*, 2016, **105**, 2527–2544.
33 S. H. Thorat, M. V. Patwadkar, R. G. Gonnade and R. Vaidhyanathan, *CrystEngComm*, 2014, **16**, 8638–8641.
34 S. Roy, R. Quiñones and A. J. Matzger, *Cryst. Growth Des.*, 2012, **12**, 2122–2126.
35 D. L. Zynger, M. J. Everton, N. D. Dimov, P. M. Chou and X. J. Yang, *Am. J. Clin. Pathol.*, 2008, **130**, 224–230.
36 C. K. Tye, C. C. Sun and G. E. Amidon, *J. Pharm. Sci.*, 2005, **94**, 465–472.
37 S. Chattoraj, L. Shi and C. C. Sun, *CrystEngComm*, 2010, **12**, 2466–2472.
38 C. C. Sun, *J. Adhes. Sci. Technol.*, 2011, **25**, 483–499.
39 S. R. Perumalla, L. Shi and C. C. Sun, *CrystEngComm*, 2012, **14**, 2389–2390.
40 N. Xu, *J. Baotou Med. Coll.*, 2018, **34**, 117–121.
41 B. Y. Ren, X. L. Dai, F. Zhang, T. X. Long, Y. L. Huang, J. M. Chen and T. B. Lu, *Cryst. Growth Des.*, 2022, **22**, 5785–5790.
42 K. Etherson, C. Dunn, W. Matthews, H. Pamelund, C. Barragat, N. Sanderson, T. Izumi, C. D. C. Mathews, G. Halbert, C. Wilson, M. McAllister, J. Mann, J. Østergaard, J. Butler and I. Khadra, *Eur. J. Pharm. Biopharm.*, 2020, **150**, 24–32.
43 Y. Wei, L. Zhang, N. Wang, P. Shen, H. Dou, K. Ma, Y. Gao, J. Zhang and S. J. Qian, *Cryst. Growth Des.*, 2018, **18**, 7343–7355.